Journal of Alloys and Compounds 1006 (2024) 176206

Contents lists available at ScienceDirect

Journal of Alloys and Compounds

journal homepage: www.elsevier.com/locate/jalcom

Ball milling and annealing effect in structural and magnetic properties of copper ferrite by ceramic synthesis

Miguel Ángel Cobos [a,*], José Antonio Jiménez [b], Irene Llorente [b], Patricia de la Presa [a,c], Antonio Hernando [a,d,e,f]

[a] Instituto de Magnetismo Aplicado (UCM-ADIF-CSIC), A6 22,500 Km, Las Rozas 28260, Spain
[b] Centro Nacional de Investigaciones Metalúrgicas (CENIM-CSIC), Avda. Gregorio del Amo, 8, Madrid 28040, Spain
[c] Department of Material Physics, Complutense University of Madrid, Madrid 28040, Spain
[d] Donostia International Physics Center, Donostia 20028, Spain
[e] IMDEA Nanociencia, Madrid 28049, Spain
[f] Engineering Department, Nebrija University, Madrid, Spain

ARTICLE INFO

Keywords:
Ceramics
Magnetically ordered materials
Solid state reactions
Magnetization
Microstructure

ABSTRACT

This study aims to better understand the relationship between the microstructure and magnetic properties of copper ferrite, which is an inverse spinel that present a body-centered tetragonal structure associated with a remarkable Jahn–Teller (JT) effect. For this goal, a sample has been synthesized by the ceramic route from a stoichiometric mixture of high-purity CuO and Fe_2O_3 powders activated mechanically in a high-energy planetary ball mill. This sample was calcined in air furnace at 1000 ºC for 6 h. As synthetized sample with a cubic structure was divided into two parts and one of them was annealed at 650 ºC for 3 h and slowly cooled to room temperature to obtain a pure tetragonal spinel sample. Furthermore, these two samples were subjected to the same processes of severe plastic deformation by milling for up to 70 h and subsequent annealing at temperatures ranging between 300 and 600 ºC to obtain samples with a mixture of phases in different proportions. For the cubic one, there is no change in its structure due to milling, always remaining 100 % cubic, and the evolution in the saturation magnetization was related to the changes in the density of defects present. On the other hand, copper cations are always found in the octahedral sites of spinel with a tetragonal structure. The small decrease in the degree of inversion to 0.95 induced by milling in this sample is capable of breaking the JT distortion, giving rise to the appearance of a cubic phase. This work demonstrates how the structure, microstructure, defects like stacking faults and deformation twins, and degree of inversion of the different phases are related to changes in magnetic properties.

1. Introduction

Ferrites of the type AFe_2O_4 (A = transition metal) have been widely studied for their fundamental properties and a broad range of technological applications [1–4]. The magnetic and physical properties of this material are strongly linked to the structure and, in particular, to the inversion degree δ. It is well known that, depending on the type of A cation and their distribution between the octahedral or tetrahedral sites, different magnetization states such as paramagnetic, antiferromagnetic, superparamagnetic, spin glass and ferrimagnetic behaviors are observed [5].

Particularly, copper ferrite has been the subject of multiple studies in the last three decades due to both theoretical issues and technological applications in a wide variety of areas such as biomedicine [6,7], water treatment [8–11], catalysis [12,13] and gas sensing [14,15]. In equilibrium at room temperature, $CuFe_2O_4$ is a totally inverse ferrite since the Fe^{3+} cations fully occupy the tetrahedral positions and Cu^{2+} cations occupy the half of the octahedral positions. The strong antiferromagnetic superexchange interactions among of Fe^{3+} cations makes the saturation magnetization is originated by the 8 Cu^{2+} at the octahedral sites. However, under certain conditions, it may occur a cation rearrangement of the type $(Fe_{\delta}^{3+}Cu_{(1-\delta)}^{2+})[Cu_{\delta/2}^{2+}Fe_{1-\delta/2}^{3+}]_2O_4$ where δ is the

* Corresponding author.
E-mail addresses: micobos@ucm.es (M.Á. Cobos), jimenez@cenim.csic.es (J.A. Jiménez), irene@cenim.csic.es (I. Llorente), pmpresa@ucm.es (P. de la Presa), antherna@ucm.es (A. Hernando).

https://doi.org/10.1016/j.jallcom.2024.176206
Received 20 May 2024; Received in revised form 23 August 2024; Accepted 27 August 2024
Available online 29 August 2024

inversion parameter. As the Cu^{2+} and Fe^{3+} exchange their positions, δ decreases and the structural and magnetic properties are strongly affected.

Many types of synthesis are reported for spinel ferrites in the literature, such as wet chemical like co-precipitation [16], hydro and solvothermal [17], sol-gel [18]; physical synthesis ceramic method or ball milling of precursors [9,13,19,20]. Ceramic methods as well as ball milling procedures have the convenience of simplicity to get high purity and quantity of product. It has been reported that depending on the synthesis route and on the further thermo-mechanical treatments, copper ferrite can crystallize in the cubic or in the tetragonal structure, but both phases can coexist in some samples [21–23]. In fully inverse structures, the degenerate electronic ground states associated with cations Cu^{2+} at octahedral positions lead to strong distortion of the coordination environment to reduce the symmetry and eliminate the degeneracy. As a result of this distortion, there is a transition from cubic to tetrahedral structure (Jahn-Taller (JT) effect) [24–27]. The different studies of magnetic properties coincides that copper ferrite with tetragonal structure reaches less saturation magnetization than with cubic one [28–30]. This makes sense since the distortion produced by the JT effect makes the intercationic distances larger and therefore a weaker superexchange interaction than in the cubic phase.

In this work, we present a detailed study on the structural and magnetic properties in a spinel copper ferrite synthetized from oxides by the standard ceramic technique. Although the tetragonal structure is thermodynamically more stable at low temperatures, the high temperature cubic structure remains after quenching to room temperature [31]. Thus, the sample was quenched in air to room temperature after the solid-state reaction at 1000 ºC to stabilize the cubic modification. On the other hand, a second-order phase transition between low-temperature tetragonal and high-temperature cubic modifications of $CuFe_2O_4$ that does not require diffusion has been reported at approximately 400 ºC [32]. It has been reported that beside α-Fe_2O_3, secondary phases like CuO, Mn_2O_3 or MgO may form in Cu, Mn-Zn and Mg ferrites, respectively [33–36], These works showed that stability of spinel ferrite phase is sensitive to factors like chemical composition, the annealing temperature and the atmosphere under the thermal treatment was performed (air, Oxygen or Argon atmosphere). Further it is also demonstrated that the presence of impurity phases give raise to a decrease of the magnetic properties, which are attributed to the depletion of Fe^{3+} from the spinel phase. The cubic spinel phase $CuFe_2O_4$ is metastable below approximately 544ºC and decomposes to $CuO+Fe_2O_3+CuFeO_2$ [31]. Therefore, a part of as-synthesized sample was annealed at 650 °C for 3 h and then slowly cooled in the furnace to room temperature to obtain a pure tetragonal spinel sample. Furthermore, samples with pure cubic and tetragonal modifications were subjected to the same processes of severe plastic deformation by milling for up to 70 h and subsequent annealing at temperatures ranging between 300 and 600 ºC to obtain samples with a mixture of phases in different proportions. In these samples, the influence of the structure, microstructure, defects such as stacking faults and deformation twins and the degree of inversion on the magnetic properties will be investigated.

2. Experimental section

Copper ferrite has been prepared by the solid-state reaction route from high purity CuO and Fe_2O_3 powders supplied by Merck and Alpha Aesar, respectively. A stoichiometric proportion of 1:1 of these precursors were grinded by 2 h in a planetary mill (at 275 rpm) to enhance the reactivity of materials during calcination [37]. The resulting powders were pelletized and calcined in air for 6 h at 1000 ºC and cooled down at air. This calcination temperature was selected considering the description at temperatures ranging from 650 to 1000ºC of the Cu-Fe-O ternary system reported by Khvan et al. [38], while the choice of both, milling and reaction times was based on the desired particle size and our previous work [39]. The as synthetized sample with the cubic structure (CS0 sample) was divided in two parts, and one of them was annealed at 650 ºC for 2 h (TS0 sample) in order to get the pure tetragonal spinel sample.

Part of the CS0 and TS0 samples were mechanical milled to study the effect of plastic deformation on the microstructure and magnetic properties of spinel copper ferrite. The samples were introduced into a stainless steel jar of 250 cm^3 together with 10 mm stainless steel grinding balls in ball-to-powder weight ratio of 10:1. This process was carried out up at room temperature in a planetary ball mill Retsch PM400 (Retsch Gmbh, Haan, Germany). The milling process was interrupted after 5, 10, 20 and 40 h. Theses samples were denotes as CSt and TSt (for example, CS20 or TS20). Milled CS40 sample was further subject to annealing treatments for 1 h at different temperatures ranging from 300 to 600 ºC. Heat treated samples were named as CS40-T (for example, CS40–300).

Microstructural characterization of the samples was performed by X-ray diffraction (XRD) using Co radiation (λ = 1.78897 Å) in a Bruker (Bruker AXS, GmbH, Karlsruhe, Germany) D8 Discover diffractometer working in parallel beam geometry (Goebel mirror). XRD spectra were recorded over an angular range of 2θ from 10 to 120º with a step of 0.015º using a LynxEye linear detector. The obtained XRD data were fitted by the Rietveld method using the version 6.0 of the analysis program TOPAS (Bruker AXS, GmbH, Karlsruhe, Germany) and a structural model containing the phases previously identified using the JCPDS data base, which crystallographic information was taken from the Pearson crystallographic database [40]. The refinement protocol used included the degree of inversion constraining the cations at the octahedral and tetrahedral sites to keep the stoichiometric value. The quality of the refinements was evaluated by the statistically expected least-squares factor (Rexp), the weighted summation of residual of the least-squares fit (Rwp), and the goodness of fit (GoF) or chi-square, whose limit tends to 1.

X-ray photoelectron spectroscopy (XPS) can be a valuable technique to characterize the chemical state of the cations present in cooper ferrites and to determine their coordination environments, i.e. the amount of Cu and Fe cations on both, tetrahedral and octahedral coordination sites. However, it should be noted that XPS is a surface-specific technique that provides information from a depth of about 2 nm and therefore not from the bulk. The chemical state of atoms and the occupancy of tetrahedral to octahedral site in the bulk crystal structure may not be the same as on the surface. For this reason, the cation distribution in the tetrahedral and octahedral sites in spinel ferrites has been deduced in most of previous works on the basis of Rietveld refinement of X ray diffraction data, and/or the intensity ratio in the Mössbauer spectra of the sextets due to Fe^{3+} cations in the tetrahedral and octahedral sites. Combined XRD and Mössbauer spectral studies have concluded that the cation distribution obtained from the X-ray intensity data agrees fairly well with the cation distribution estimated from Mössbauer data [41,42]. Considering that the diffraction profile analysis with the Rietveld method allows simultaneously getting the relevant information of the material microstructure, it was selected the use of X ray diffraction for this goal in this work.

On the other hand, the magnetometric study of the samples was carried out using a standard superconducting quantum interference device (SQUID) MPMS (Quantum Design, GmbH, Darmstadt, Germany). Zero field cooled (ZFC) and field cooled (FC) measurements were taken at 100 Oe between 5 and 300 K. In addition, hysteresis cycles were measured at 5 and 300 K and at 5 T as maximum applied field.

Scanning electron microscopy (SEM) and transmission electron microscopy (TEM) have been used to study the morphology and size of the particles in the different samples and energy dispersive X-ray spectroscopy (EDX) to quantify the elements present. The images used for this characterization were obtained using the equipment JEOL JSM 6335 F, JEOL JEM3000F and JEOL JEM2100. On the other hand, high resolution TEM (HRTEM) images were recorded to corroborate experimentally the existence of defects like stacking fault introduced in the perfect spinel

lattice as consequence of the plastic deformation during the milling process.

Calorimetric studies of thermogravimetric analysis (TG) and differential scanning calorimetric (DSC) have been performed by equipment SDT Q600 V8.3 Build 101, with a ramp method of 10 ºC/min for a sample of 10 mg, from RT to 1000 ºC at N_2 atmosphere.

3. Results

3.1. Microstructural results

Fig. 1(a) and (b) shows the XRD recorded in as-prepared CS0 and TS0 samples, respectively. The major phase present in the patterns was confirmed to be the cubic and tetragonal spinel copper ferrite by matching the XRD pattern with the JCPDS cards 01–077–0010 and 00–034–0425, respectively. Some impurity of CuO (JCPDS card no. 00–048–1548) appears for the CS0 sample, whereas TS0 sample show small amount of delaffosite $CuFeO_2$ (JCPDS card no.00–039–0246).

Quantitative phase analysis of these XRD patterns using Rietveld refinement showed that the amount of CuO and delaffosite in the CS0 and TS0 samples represent about 3.53 % and 13 %, respectively. Diffraction peaks of these two phases disappear after 10 h of milling, as shows in Fig. 2(a) and (b), but whereas in the CS10 sample all diffraction peaks correspond to the cubic $CuFe_2O_4$, the diffraction peaks of the tetragonal and cubic $CuFe_2O_4$ are present in the TS10 sample. In TSt samples, it was observed that the relative content of the cubic phase increases with milling time, and after 70 h milling only the cubic structure was detected, as shown in Fig. 2(c).

A closer inspection of the simulated diffraction patterns obtained by the Rietveld refinement shows that the shape of the peaks corresponding to the cubic phase cannot be reproduced correctly when the double Voigt method is used for the line broadening analysis. It is observed a peculiar (hkl) anisotropic line broadening, but also the presence of peak shift and asymmetry in some reflections, as shown in Fig. 3(a) for the CS40 sample. This complex shape observed for the diffraction peaks may arise due to the presence of planar faults, such as stacking or twin faults. In spinel, oxygen framework is an almost perfect FCC packing in the <111> direction, with the cations interspersed between the ABCABCABC anion layers. Mechanical milling introduced severe plastic deformation into the spinel structure. Although dislocations should slip twice the anion-anion spacing in a <110> direction, they dissociate into two collinear half-partials a/2 <1 1 0>→a/4 <1 1 0> + a/4 <1 1 0> on the slip planes because the oxygen anion is very well fixed in the intermediate positions [43]. The milling process produces a high dislocation density and thus stacking faults are introduced in the slip plane occupy by oxygen in wrong positions.

The anisotropic peak broadening may arise due to the presence of stacking faults and/or twin faults. The most widely used method for determining stacking parameters from diffraction data is the pattern simulation based on the different stacking faults and fault probabilities that may be present in the crystal lattice. The goodness of the fit is usually reduced to a visual comparison between the calculated curves and the measured intensity distributions along the different Bragg reflection, with manual retuning of the parameters to reach the best fit. However, a very good fit between experimental and calculated patterns may not be an evidence for the correctness of the used model since different kinds of faults can give rise to the same local layers' stacking (i.e. the same diffracted intensity distribution). In the inverse spinel structure, the fault with lowest energy which do not disturb stoichiometry correspond to the displacement vector a/4<110>on the fault planes, which is completely equivalent to a pure shear along the (110) a/4 [1$\bar{1}$2] direction [44]. As it can be very difficult or even impractical to extract quantitative stacking information from the diffraction pattern via a nonlinear least squares refinement of calculated pattern to the experimental data, this approach was not used for the study of structural properties of copper ferrite. Moreover a better Rietveld refinement was obtain by applying the phenomenological Stephens model for anisotropic line broadening motivated by the grinding process, as shown in Fig. 3(b). In this refinement, the average microstructural parameters, such as crystallite size and microstrain, were determined using the double-voigt approach [45]. The results obtained are shown in Tables 1 and 2 for CSt and TSt samples, respectively.

In previous works, we have related the magnetic properties of spinel zinc ferrite with the structural disorder present, which was characterized by the degree of inversion [40,46]. For the cubic phase, it was determined from the Rietveld refinement of the XRD data an inversion degree of about 0.95 and lattice parameter close to 0,8390 nm in both milled and annealed samples. On the other hand, XRD patterns of the CS40 samples annealed up to 600 ºC does not showed the reappearance of minor phases like Fe_2O_3 CuO and/or $CuFeO_2$. Thus, the evolution of its magnetic properties during grinding and after successive thermal treatments cannot be explained exclusively by considering the misplacement of the cations. Defects like stacking or twin faults induced by mechanical milling have to be also considered. When two oxygen layers slip along each other in copper ferrite, the octahedral ions between them have to move to another octahedral position to avoid the formation of a new type of cation layer, changing the distance between the octahedral ions and its neighbors. As shown in Tables 1 and 2, crystallite size decrease with milling time, tending to saturate to 8–10 nm. However, microstrain follows a different trend, with a rapid increase in the initial stage of the grinding process. Formation of both stacking faults and twin faults restricts the dislocation mobility, resulting high dislocation densities which increases stored energy. After a certain grinding time, it was observed a decrease on the microstrain. The long milling would promote the formation of new grains boundaries to release part of the energy stored during extensive deformation,

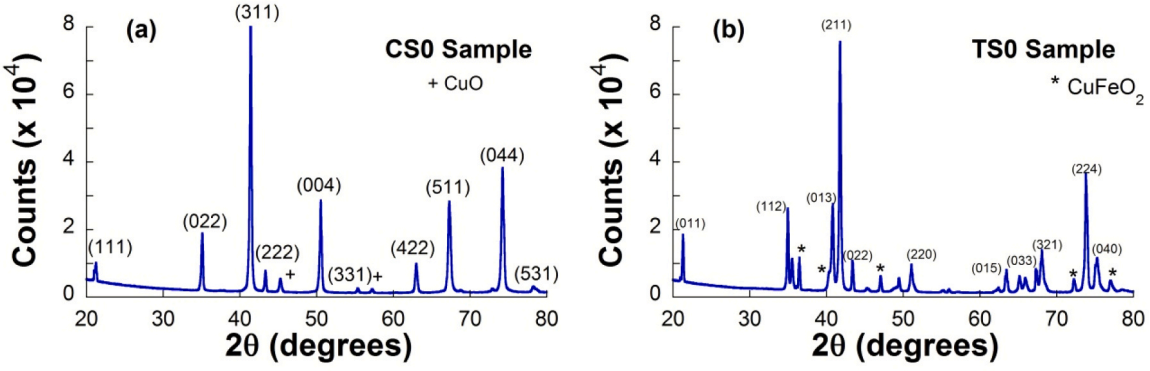

Fig. 1. XRD patterns: (a) CS0 and (b) TS0 samples. Tenorite phase marked by + in the XRD pattern of the CS0 sample while delaffosite as * in the XRD pattern of the TS0 sample.

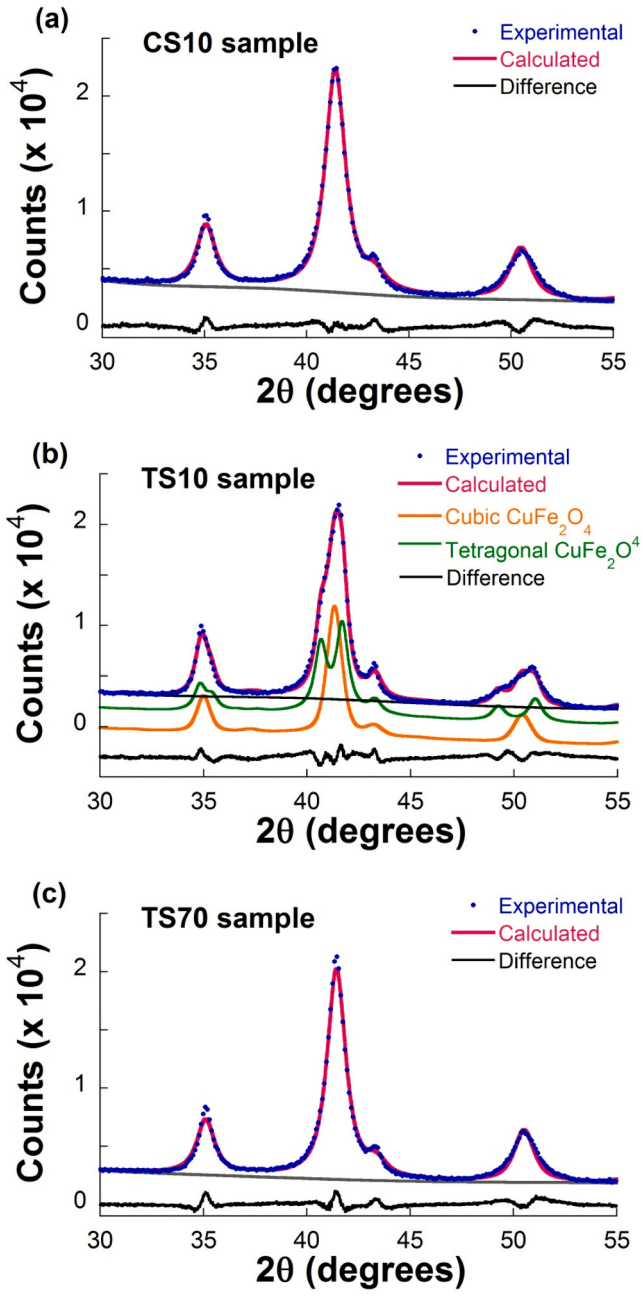

Fig. 2. Results of Rietveld refinements of the XRD patterns: (a) CS10, (b) TS10 and (c) TS70 samples. The differences between experimental data (blue dots) and the fitted simulated pattern (red line) are plotted as a continuous black line at the bottom.

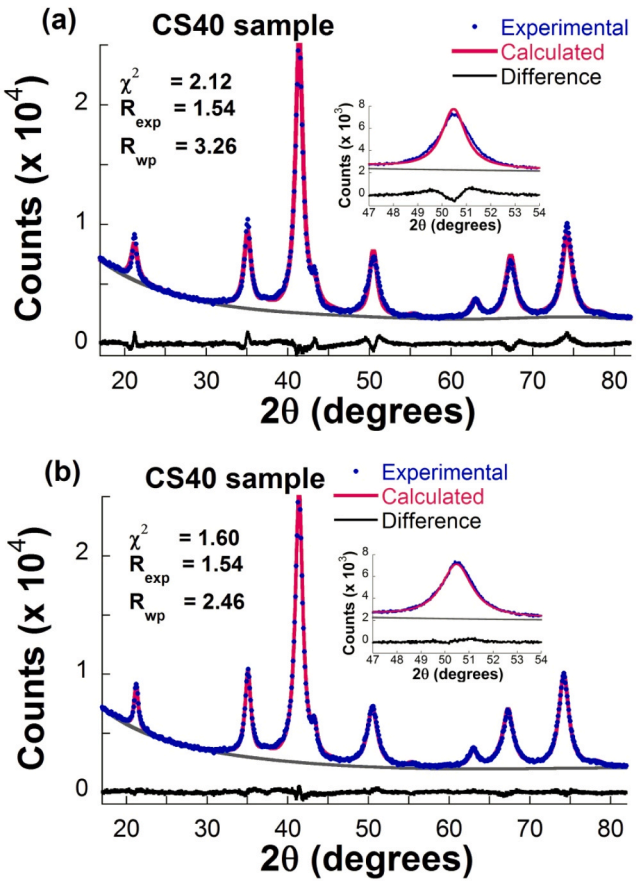

Fig. 3. Results of Rietveld refinements of the XRD data of sample CS40: (a) considering only the size-strain line-broadening given by the Double Voigt approach and (b) including also an anisotropic diffraction-line broadening according to the Stephen's model. The difference between the experimental (blue dots) and the fitted simulated (red line) patterns are plotted as a continuous black line at the bottom.

decreasing the crystalline imperfections generated in the material during milling with dislocations being the major contributor. On the other hand, annealing caused the recovery and recrystallization of the structure and the gradual appearance of the tetragonal phase.

SEM images of CS40 and TS40 samples presented in Fig. 4(a) and (b) show that these materials are formed by spherical powders of nanoparticle agglomerates. The bright-field TEM micrograph shown in Fig. 5 for the CS40 sample reveals nanosized particles with polygonal/spheroidal shapes and a diameter close to the crystallite size determined from XRD patterns (~ 10 nm).

HRTEM images obtained from CS10 sample show that many particles contain numerous stacking faults due to severe plastic deformation during high energy ball milling. The square red area of around 10×10 nm selected in Fig. 6(a) is shown in detail in Fig. 6(b). In this figure, it can be observed by red lines the discontinuity of interplanar lines caused by the stacking faults during milling process. This confirmed that the asymmetry observed in the corresponding XRD profile is due to the presence of planar defects in the sample.

Semi-quantitative energy-dispersive X-ray microanalysis was performed in a SEM at randomly selected regions of the CS10, CS40 and TS40 samples for testing their homogeneity and chemical composition.

Table 1
Microstructural parameters obtained from the Rietveld refinement of the diffraction patterns recorded for the CSt samples. The standard deviations are in parenthesis.

Sample Name	Phase content	Size crystallite (nm)	microstrain	Tetrahedral occupancy of Fe^{3+}
CS0	C100 %	50(5)	0.0004(1)	0.95(1)
CS10	C100 %	10(1)	0.0030(3)	0.94(1)
CS20	C100 %	10(1)	0.0022(2)	0.94(1)
CS40	C100 %	11(1)	0.0021(2)	0.94(1)
CS40–300	C100 %	10.5(1)	0.0020(2)	0.94(1)
CS40–400	C56 %	13(1)	0.0038(4)	0.93(1)
	T44 %	12(1)	0.0030(3)	1.00(1)
CS40–500	C57 %	17(2)	0.0030(3)	0.93(1)
	T43 %	13(1)	0.0029(3)	1.00(1)
CS40–600	C51 %	60(6)	0.0031(3)	0.88(1)
	T49 %	13(1)	0.0018(2)	1.00(1)

Table 2
Microstructural parameters obtained from the Rietveld refinement of the diffraction patterns recorded for the TSt samples. The standard deviations are in parenthesis.

Sample	Phase content	Size crystallite (nm)	microstrain	Tetrahedral occupancy of Fe^{3+}
TS0	T100 %	>150	0.0005(1)	1.00(1)
TS10	C46 %	17(2)	0.0032(3)	0.92(1)
	T54 %	19(2)	0.0015(1)	1.00(1)
TS20	C54 %	12(1)	0.0028(3)	0.94(1)
	T46 %	18(2)	0.0018(2)	1.00(1)
TS40	C66 %	9(1)	0.0024(2)	0.92(1)
	T34 %	10(1)	0.0026(2)	1.00(1)
TS70	C100 %	8(1)	0.0015(1)	0.98(1)

Atomic per cent of the Fe and Cu are listed in Table 3. Taking into account precisions of EDX analyses, this table shows that the actual composition of milled powders is maintained close to the nominal composition. However, due to the very small size of the particles shown in Fig. 5 and crystallite sizes reported in Tables 1 and 2, these values will include information of several particles since the spatial resolution associated with a SEM-EDX analysis is higher than 1 μm. There are several techniques for creating nanoscale maps of elemental composition, like nanoscale secondary ion mass spectrometry (NanoSIMS) or scanning transmission electron microscope (STEM) image and EDX maps, which will be considered as the following step in the close future.

3.2. Thermal results

The differential scanning calorimetry (DSC)/ Thermogravimetric analysis (TGA) curves of samples with the cubic and tetragonal structure milled for 40 h (CS40 and TS40 samples, respectively) are depicted in Fig. 7(a) and (b). In this figure, the TGA curves (in black) of these two samples show two weight losses. The first one is observed between room temperature and 400 ºC. A similar result is reported by Younes et al. [47], who related this weight loss to the evaporation of water. On the other hand, another temperature interval of weight loss occurs between 750 and 1000 ºC. This second weight loss was associated with the thermal decomposition of a small amount of $CuFe_2O_4$ at high temperatures due to the loss of oxygen and the partial reduction of Cu^{2+} to Cu^{+1} [48]. For this reason, it can be observed the presence of traces of CuO and $CuFeO_2$ in as-synthetized CS0 and TS0 samples in Fig. 1. Finally, it is worth noting that no considerable weight loss took place in this temperature range since the weight loss in Fig. 7 is about 3 % for both samples. Therefore, no significant changes in magnetic moments are expected associated to the presence of secondary phases.

According to the obtained results of DSC measurements shown in red in Fig. 7, in our case is difficult to determine a phase transformation between tetragonal and cubic crystal structures during heating from the

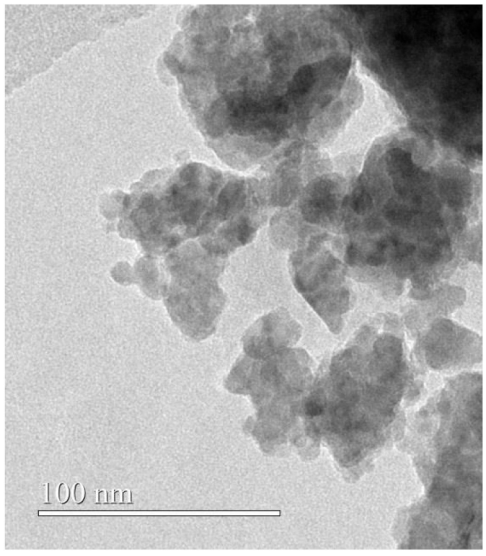

Fig. 5. TEM micrograph of CS40 sample.

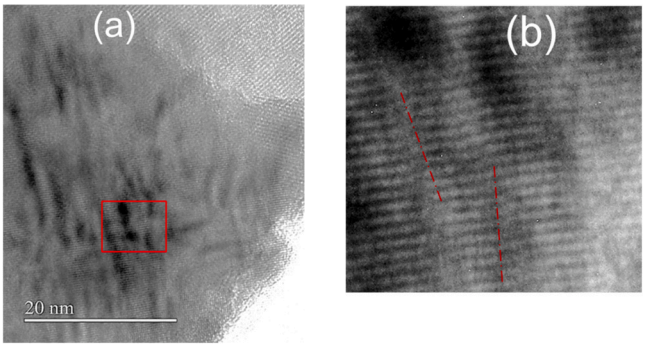

Fig. 6. HRTEM images: (a) CS10 sample and (b) red square detail showings stacking faults produced by the milling process.

Table 3
Semi-quantitative elemental composition of various samples obtained from SEM-EDX spectra. The standard deviations are in parenthesis.

Sample	Fe (atomic %)	Cu(atomic %)
CS10	66(4)	34(4)
CS40	62(4)	38(4)
TS40	66(4)	34(4)

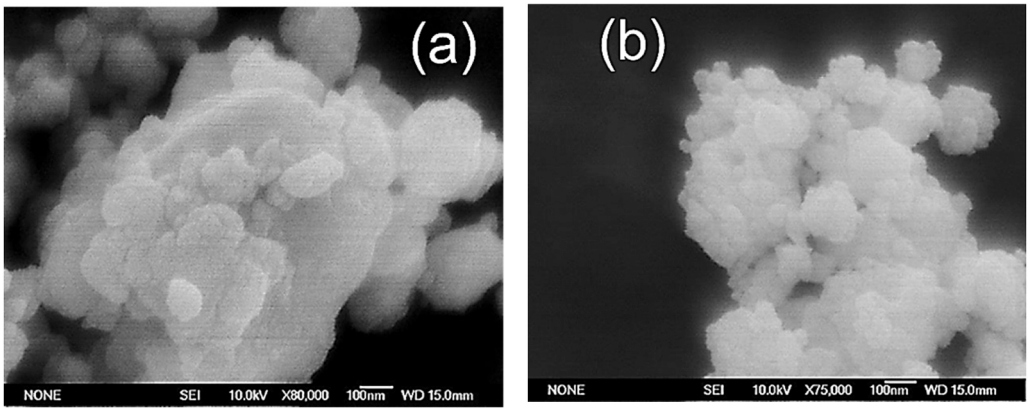

Fig. 4. SEM images: (a) CS40 and (b) TS40 samples.

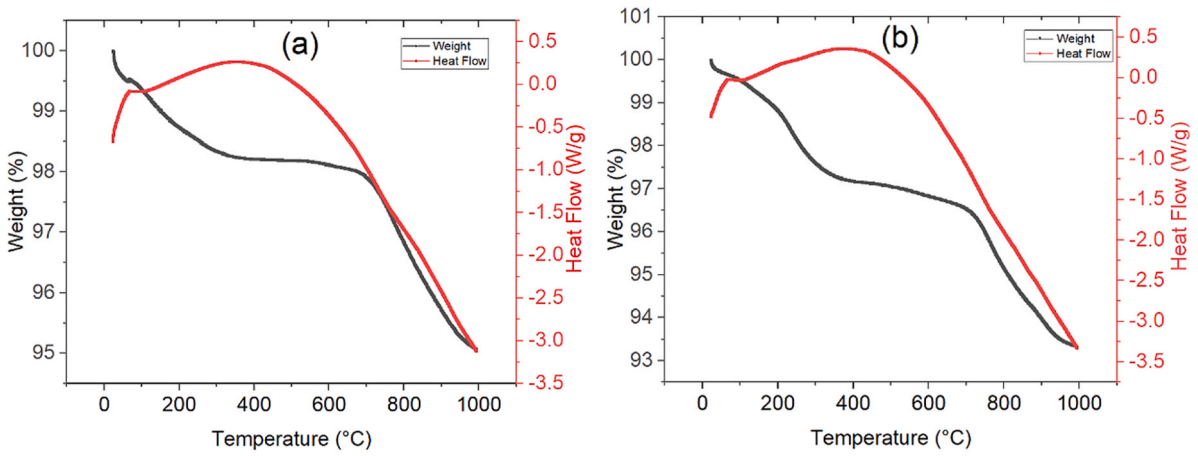

Fig. 7. TG (black) and heat flow (red) curves obtained in samples milled for 40 h: (a) SC40 and (b) TS40 samples.

DSC curves, as expected in a second-order phase transition like the phase transition between tetragonal and cubic modifications of Cu spinel. In general, well-defined peaks can be observed for first-order transitions, while second-order transitions are characterized by variations in the heat flow curve. Thus, the transition should be monitored in a future work by the examination the evolution of the lattice parameters as a function of temperature using high-temperature X-ray diffraction, looking for the temperature at which the tetragonal splitting is lost and the pattern can be indexed to a face-centered cubic cell.

3.3. Magnetic results

Figs. 8 and 9 show the hysteresis curves at 5 and 300 K in for the CSt and TSt samples, respectively.

There are markedly differences in the magnetic parameters for all the samples. As synthesized CS0 sample has around 20 % higher magnetization than the TS0 sample, however, after 10 h of milling, both samples reach similar Ms values. This value corresponds to the minimum magnetization reached by any sample of the CSt serie, but in the case of the TSt samples the minimum value of Ms is only reached after 40 h of milling, as shown in Table 4. After this minimum, a progressive increase in magnetization is observed in both, CS and TS samples. Finally, a value similar to that measured in sample CS0 was found after 40 and 70 h for CS40 and TS70 samples, respectively. On the other hand, the coercitivity is quite similar for CSt and TSt samples.

Table 5 shows experimental and theoretical magnetic moments as a function of inversion degree for CSt samples. Theoretical calculations have been done using the site occupancy factors obtained from the Rietveld refinement and considering values of 5.92 and 1.73 μ_B for the magnetic moments of Fe^{3+} and Cu^{+2} cations, respectively. With the exception of the as-synthesized CS0 sample, Table 5 shows remarkable differences between experimental and theoretical values. Although according to Table 1 the CSt samples have a pure cubic structure until 40 h of milling and similar values for the inversion degree, the evolution of the experimental values of Ms with milling time would indicate that there must be additional parameters affecting the magnetization.

Table 4 also shows that annealing the CS40 sample at temperatures above 400 °C causes a decrease in magnetization. This treatment induced the phase transformation from the cubic to tetragonal phase and an increase in the microstrain of the cubic phase (see Table 1). Thus, it was concluded that Ms depends on both cubic and tetragonal phases and the formation of stacking faults associated with an increase on the dislocation density.

4. Discussion

Microstructural factors that may influence on the variation of Ms are mainly: phase type (cubic or tetragonal, and its average if it is mix), inversion degree, particle size and structural defects as stacking faults [49]. Inversion degree is directly responsible for the net magnetization produced by the antiferromagnetic coupling between cations in the tetrahedral and octahedral sublattices. Since perfect inverse copper ferrite has δ =1, any decrease of δ should lead to an increase of the magnetization. We were not able to obtain δ =1, and a maximum value

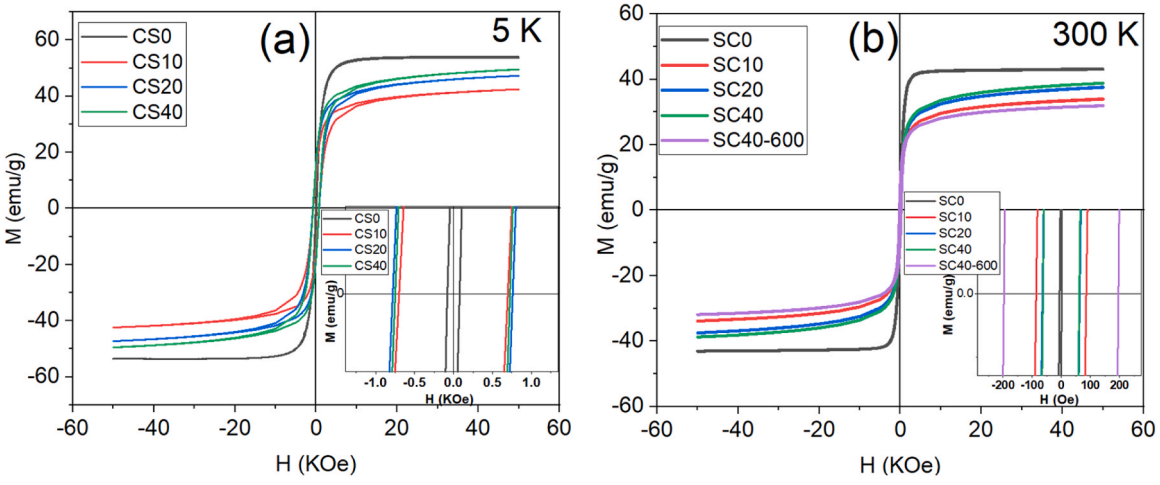

Fig. 8. Hysteresis curves for CSt samples: (a) at 5 K and (b) at 300 K.

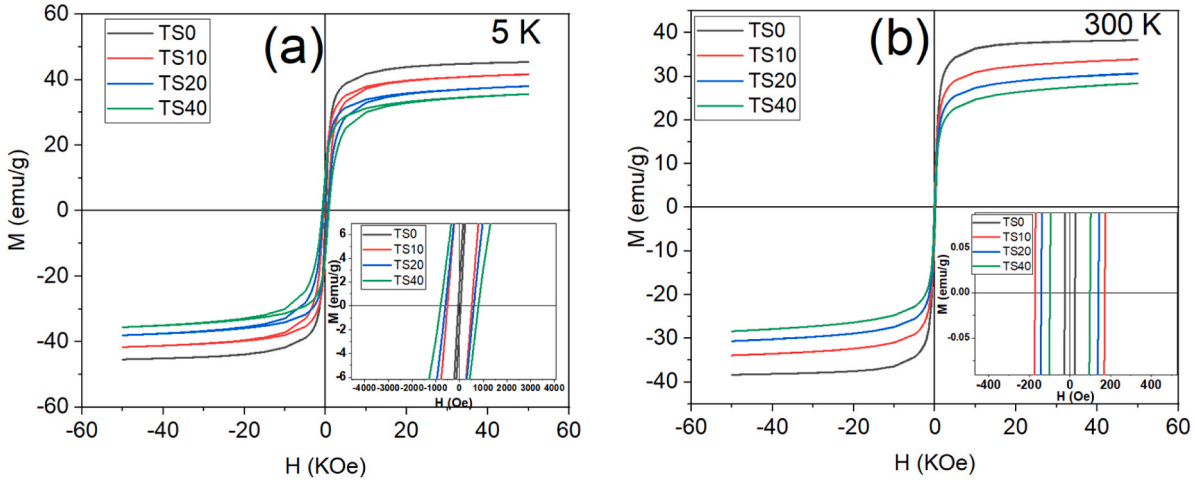

Fig. 9. Hysteresis curves for TSt samples: (a) at 5 K and (b) at 300 K.

Table 4
Magnetic results of CSt and TSt samples. Saturation magnetization (Ms) and coercivity (Hc) at 5 and 300 K are given in emu/g and Oe, respectively. The standard deviations are in parenthesis.

CS Samples	5 K		300 K		TS samples	5 K		300 K	
	Ms	Hc	Ms	Hc		Ms	Hc	Ms	Hc
CS0	53(1)	80(1)	43(1)	0	**TS0**	45(1)	50(1)	38(1)	25(1)
CS10	42(1)	700(7)	34(1)	85(1)	**TS10**	42(1)	500(5)	34(1)	175(2)
CS20	47(1)	800(8)	37(1)	60(1)	**TS20**	38(1)	600(6)	31(1)	140(1)
CS40	49(1)	750(8)	39(1)	60(1)	**TS40**	36(1)	800(8)	28(1)	100(1)
CS40–300	48(1)	800(8)	39(1)	50(1)	**TS70**	54(1)	700(7)	42(1)	65(1)
CS40–400	30(1)	810(8)	27(1)	150(2)					
CS40–500	34(1)	500(5)	30(1)	120(2)					
CS40–600	34(1)	550(5)	31(1)	200(2)					

Table 5
Experimental and theoretical magnetization values for CSt samples. The standard deviations are in parenthesis.

	Experimental data		Calculated values		
Sample	μ_B	emu/g	δ	μ_B	emu/g
CS0	2.3	53(1)	0.95	2.3	50
CS10	1.8	42(1)	0.94	2.2	52
CS20	2.0	47(1)	0.93	2.3	54
CS40	2.1	49(1)	0.93	2.3	54

of 0.95 was reached for the as-synthesized sample CS0. This inversion degree value does not decrease very much after 40 h of milling (from 0.95 to 0.94). This indicates there is not enough energy with the planetary speed of 275 rpm to move Fe cations from octahedral to tetrahedral sites of the spinel crystal as it is possible in direct ferrite like zinc ferrite in the same milling conditions [46].

For the CS0 sample, the Ms at 5 K is 53 emu/g, in good agreement inside the experimental errors with the theoretical values given in Table 5. The saturation magnetization Ms at 5 K decreases with increasing grinding time, but due to an expected decrease in inversion degree as grinding time increases, theoretically the saturation magnetization should increase. Table 5 shows a significant decrease in Ms after 10 h of milling followed by a continuous increase in magnetization up to the initial value for higher times, although δ remains practically constant. Therefore, there are additional effects that are affecting the magnetic properties.

The Rietveld refinement with Stephens's phenomenological model of anisotropic strain (Fig. 4(b)), confirms the presence of defects in the crystal like stacking faults and/or twin faults that tend to decrease the magnetization. When two oxygen layers displace along each other, the octahedral ions between them have to move to another octahedral position to avoid the formation of a new type of cation layer, changing the distance between the octahedral ions and its neighbors, leading to a decrease of the magnetization.

For a better understand of the behavior of Ms evolution of CS samples in their full itinerary (disorder by grinding and order by annealing), Fig. 10 includes 4 stages during the milling and annealing processes. At the beginning of the milling (Stage I), it is observed a very sharp drop caused by a continuous increase of planar defects like staking faults that arise from plastic deformation induced by mechanical milling. The ferrimagnetism of crystals of the spinel type is determined by superexchange interaction between cations at the tetrahedral and octahedral positions. Generally, the interaction energy depends on the distances between the cations and oxygen anions and the angle formed by the M-O-M′ bonds. As the formation of a stacking fault changes the distance between the octahedral ions in the new position and its neighbors, these two parameters will be disturbed, explaining the observed decrease on the Ms in the Fig. 10 after 10 h milling. This phenomenon has been studied before for material such as palladium and nickel [49–51]. Fig. 10 shows a partial recovery of the Ms value for longer grinding times (Stage II). Long milling would promote the reduction of crystalline defects, mainly dislocations generated in the material by the severe plastic deformation that accompanies this process by forming new grain boundaries to release part of the stored energy (dynamic recovery). Thus, it is observed a decrease on microstrain value in Table 1 in the samples milled for more than 20 h. The Ms value reached after 40 h milling is conserved after annealing at 300 °C since at this temperature the cation diffusion is too slow. As cations are frozen on their sites, the defect structure remains basically unchanged. The velocity of the cation rearrangement in cooper ferrite is rapid above 400 °C [52]. This temperature coincides with the tetragonal-cubic transition of

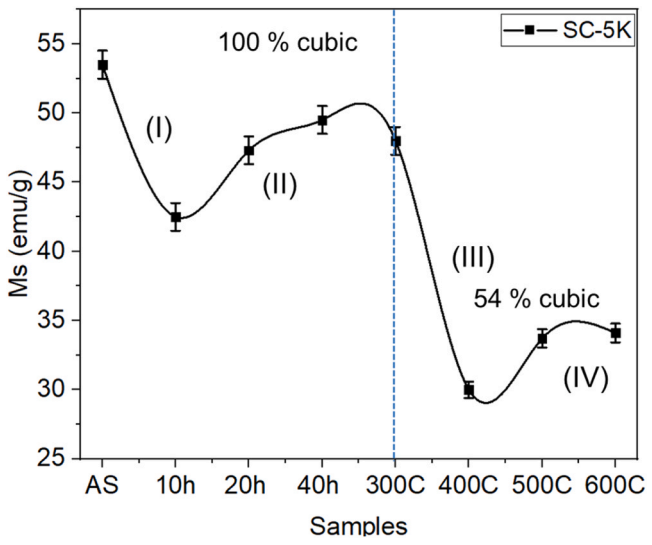

Fig. 10. Evolution of Ms at 5 K as a function of milling time in CSt samples and annealing temperature from 300 to 600 ºC in the CS40 sample.

a material slowly cooled to room temperature. As the cubic to tetragonal phase transition in $CuFe_2O_4$ is accompanied by a noticeably increase in cell volume, it must be accommodated by the generation and motion of dislocations, and therefore stacking faults and twin faults, in the surrounding cubic structure, leading to the microstrain increase observed in Table 1 for the CS40–400 sample. Thus, a new sharp drop is observed in Fig. 10 when samples are annealed at 400 ºC (Stage III), Finally at 500 and 600 ºC (Stage IV) an increase of Ms is produced because the increase of particle size and a decrease of the defects density associated with the recrystallization process of the cubic phase.

Copper ion having an odd number of electrons has all the energy levels degenerated with Kramers degeneration [53]. But as is well known in any nonlinear assembly of electrons the only possible degeneracy of a steady state is the Kramers one. As the *d* subspace is split under octahedral or tetrahedral environment in the two subspaces e_g and $t_{2\,g}$, the configuration d^9 is necessarily degenerated as concerns the orbital part of the wave function. To eliminate this degeneracy, the environment is elastically deformed up to split the lower energy subspace giving rise to an orbital singlet, in which the remaining degeneracy is only due to the spin, i. e. Kramers degeneracy.

However, the crystal field splitting for the same charge and distances to the first neighbors ligands is different for octahedral and tetrahedral environment, being for the tetrahedral symmetry 0.4 times the corresponding one for the octahedral one. This difference could explain a subsequent difference in the Jahn-Teller strain induced by Cu ion in A and B sublattices. When all the Cu atoms are located at the B sublattice, $\delta=1$, the Jahn-Teller distortion is uniform over the whole sample that, in this case, holds tetragonal symmetry. However, as Cu atoms migrate to A sublattice the local Jahn-Teller strain fluctuates in strength through the crystal. This heterogeneous strain distribution may be in the origin of formation of a cubic symmetry and the appearance of stacking faults, experimentally detected and that would contribute to the decrease in magnetization observed experimentally and that was unexpected by considering simply a δ decrease. Note that as δ decreases an increase in the magnetization is expected.

5. Conclusions

In conclusion, two copper ferrites have been obtained by solid state ceramic synthesis with pure cubic and tetragonal structures respectively, with different calcination temperatures and cooling rates.

The ferrite with the cubic structure maintains this structure when subjected to a milling process of up to 40 h. During this milling process, it is induced an increase of the defects density associated with plastic deformations, which have been analyzed by X ray diffraction and by HRTEM microscopy. This characterization study showed the presence of planar defects like stacking faults, which produces a drastic fall in the saturation magnetization in the first 10 h of milling to later undergo a recrystallization process of the microstructure that causes the recovering of part of the lost saturation magnetization. However, the applied energy of milling is not enough to decrease the degree of inversion less than 0.94. On the other hand, when an annealing treatment above 400 ºC is carried out in milled samples, it is induced the phase transformation from the cubic to tetragonal phase.

The tetragonal ferrite is produced by the Jahn-Teller (JT) effect and it is found that all its copper cations are always in the octahedral sites of the spinel due to its inversion degree is 1. When subjected to a disordering process by milling it gives rise to the appearance of a cubic phase with a small decrement of inversion degree (0.95), but enough to break the JT effect.

CRediT authorship contribution statement

José Antonio Jiménez: Validation, Methodology, Formal analysis, Conceptualization. **Miguel Angel Cobos:** Writing – review & editing, Writing – original draft, Validation, Investigation, Formal analysis, Data curation. **Patricia de la Presa:** Writing – review & editing, Validation, Supervision. **Irene Llorente:** Investigation. **Antonio Hernando:** Writing – review & editing, Validation.

Declaration of Competing Interest

The authors declare that they have no known competing financial interests or personal relationships that could have appeared to influence the work reported in this paper.

Data Availability

Data will be made available on request.

Acknowledgements

This work was supported by the Ministerio de Ciencia e Innovacion de España (Grant IDs. PID2021-123112OB-C21, PDC2022-133039-I00, TED2021-129688B-C21, PID2021-126166OB-I00, PID2022-138332NB-C41).

References

[1] M. Sugimoto, The past, present, and future of ferrites, J. Am. Ceram. Soc. 82 (1999) 269–280, https://doi.org/10.1111/j.1551-2916.1999.tb20058.x.
[2] A. Goldman, Modern Ferrite Technology, Second Ed., Springer Science+Business Media, Inc., New York, 2006.
[3] R. Valenzuela, Novel applications of ferrites, Phys. Res. Int. (2012) article 591839, 10.1155/2012/591839.
[4] V.G. Harris, A. Geiler, Y. Chen, S.D. Yoon, M. Wu, A. Yang, Z. Chen, P. He, P. V. Parimi, X. Zuo, C.E. Patton, M. Abe, O. Acher, C. Vittoria, Recent advances in processing and applications of microwave ferrites, J. Magn. Magn. Mater. 321 (2009) 2035–2047, https://doi.org/10.1016/j.jmmm.2009.01.004.
[5] M.A. Willard, Y. Nakamura, D.E. Laughlin, M.E. McHenry, Magnetic properties of ordered and disordered spinel-phase ferrimagnets, J. Am. Ceram. Soc. 82 (1999) 3342–3346, https://doi.org/10.1111/j.1151-2916.1999.tb02249.x.
[6] L. Khanna, G. Gupta, S.K. Tripathi, Effect of size and silica coating on structural, magnetic as well as cytotoxicity properties of copper ferrite nanoparticles, Mater. Sci. Eng. C 97 (2019) 552–566, https://doi.org/10.1016/j.msec.2018.12.051.
[7] N. Sanpo, J. Wang, C. Wen, C. Berndt, Multifunctional spinel ferrite nanoparticles for biomedical application, in: A. Tiwari, L. Uzun (Eds.), Advanced Functional Materials, 2015, John Wiley and Sons, N.J, 2015, pp. 183–218, https://doi.org/10.1002/9781118998977.ch4.
[8] C. Moreno-Castilla, M.V. López-Ramón, M.A. Fontecha-Cámara, M.A. Álvarez, L. Mateus, Removal of phenolic compounds from water using copper ferrite nanosphere composites as fenton catalysts, article 901, Nanomaterials 9 (2019), https://doi.org/10.3390/nano9060901.

[10] Y.J. Tu, C.F. You, C.K. Chang, S.L. Wang, T.S. Chan, Arsenate adsorption from water using a novel fabricated copper ferrite, Chem. Eng. J. 198–199 (2012) 440–448, https://doi.org/10.1016/j.cej.2012.06.006.

[11] K.K. Kefeni, B.B. Mamba, T.A. Msagati, Application of spinel ferrite nanoparticles in water and wastewater treatment: a review, Sep. Purif. Technol. 188 (2017) 399–422, https://doi.org/10.1016/j.seppur.2017.07.015.

[12] B.I. Kharisov, H.R. Dias, O.V. Kharissova, Mini-review: ferrite nanoparticles in the catalysis, Arab. J. Chem. 12 (2019) 1234–1246, https://doi.org/10.1016/j.arabjc.2014.10.049.

[13] M.M. Rashad, R.M. Mohamed, M.A. Ibrahim, L.F.M. Ismail, E.A. Abdel-Aal, Magnetic and catalytic properties of cubic copper ferrite nanopowders synthesized from secondary resources, Adv. Powder Technol. 23 (2012) 315–323, https://doi.org/10.1016/j.apt.2011.04.005.

[14] S. Singh, B.C. Yadav, R. Prakash, B. Bajaj, J.R. Lee, Synthesis of nanorods and mixed shaped copper ferrite and their applications as liquefied petroleum gas sensor, Appl. Surf. Sci. 257 (2011) 10763–10770, https://doi.org/10.1016/j.apsusc.2011.07.094.

[15] E.R. Kumar, R. Jayaprakash, G.S. Devi, P.S.P. Reddy, Magnetic, dielectric and sensing properties of manganese substituted copper ferrite nanoparticles, J. Magn. Magn. Mater. 355 (2014) 87–92, https://doi.org/10.1016/j.jmmm.2013.11.051.

[16] T.M. Hammad, J.K. Salem, A.A. Amsha, N.K. Hejazy, Optical and magnetic characterizations of zinc substituted copper ferrite synthesized by a co-precipitation chemical method, J. Alloy. Compd. 741 (2018) 123–130, https://doi.org/10.1016/j.jallcom.2018.01.123.

[17] J. Kurian, M.J. Mathew, Structural, optical and magnetic studies of CuFe2O4, MgFe2O4 and ZnFe2O4 nanoparticles prepared by hydrothermal/solvothermal method, J. Magn. Magn. Mater. 451 (2018) 121–130, https://doi.org/10.1016/j.jmmm.2017.10.124.

[18] P.P. Hankare, K.R. Sanadi, R.S. Pandav, N.M. Patil, K.M. Garadkar, I.S. Mulla, Structural, electrical and magnetic properties of cadmium substituted copper ferrite by sol–gel method, J. Alloy. Compd. 540 (2012) 290–296, https://doi.org/10.1016/j.jallcom.2012.06.018.

[19] E. Manova, T. Tsoncheva, D. Paneva, M. Popova, N. Velinov, B. Kunev, K. Tenchev, I. Mitov, Nanosized copper ferrite materials: mechanochemical synthesis and characterization, J. Solid State Chem. 184 (2011) 1153–1158, https://doi.org/10.1016/j.jssc.2011.03.035.

[20] G. Goya, H. Rechenberg, J. Jiang, Structural and magnetic properties of ball milled copper ferrite, J. Appl. Phys. 84 (1998) 1101–1108, https://doi.org/10.1063/1.368109.

[21] E. Prince, R. Treuting, The structure of tetragonal copper ferrite, Acta Crystallogr. 9 (1956) 1025–1028, https://doi.org/10.1107/S0365110X56002977.

[22] A.B. Ghumare, M.L. Mane, S.E. Shirsath, K.S. Lohar, Role of pH and sintering temperature on the properties of tetragonal–cubic phases composed copper ferrite nanoparticles, J. Inorg. Organomet. Polym. Mater. 28 (2018) 2612–2619, https://doi.org/10.1007/s10904-018-0927-3.

[23] X.X. Tang, A. Manthiram, J. Goodenough, Copper ferrite revisited, J. Solid State Chem. 79 (1989) 250–262, https://doi.org/10.1016/0022-4596(89)90272-7.

[24] M.H. Abdellatif, C. Innocenti, I. Liakos, A. Scarpellini, S. Marras, M. Salerno, Effect of Jahn-Teller distortion on the short range magnetic order in copper ferrite, J. Magn. Magn. Mater. 424 (2017) 402–409, https://doi.org/10.1016/j.jmmm.2016.10.110.

[25] T. Tanaka, M. Chiba, H. Okimura, Y. Koizumi, Jahn-Teller effect of Cu-ferrite films by solid reaction, J. Phys. IV Fr. 7 (1997) C1-501–C1-502, https://doi.org/10.1051/jp4:19971205.

[26] S. Kimura, T. Mashino, T. Hiroki, D. Shigeoka, N. Sakai, L. Zhu, Y. Ichiyanagi, Effect of heat treatment on Jahn–Teller distortion and magnetization in Cu ferrite nanoparticles, Thermochim. Acta 532 (2012) 119–122, https://doi.org/10.1016/j.tca.2011.09.018.

[27] K.I. Kugel, D. Khomskiĭ, The Jahn-Teller effect and magnetism: transition metal compounds, Sov. Phys. Uspekhi 25 (1982) 231–256, https://doi.org/10.1070/PU1982v025n04ABEH004537.

[28] J. Calvo-de la Rosa, M. Segarra, Influence of the synthesis route in obtaining the cubic or tetragonal copper ferrite phases, Inorg. Chem. 59 (2020) 8775–8788, https://doi.org/10.1021/acs.inorgchem.0c00416.

[29] R.S. Yadav, J. Havlica, J. Masilko, L. Kalina, J. Wasserbauer, M. Hajdúchová, V. Enev, I. Kuřitka, Z. Kožáková, Cation migration-induced crystal phase transformation in copper ferrite nanoparticles and their magnetic property, J. Supercond. Nov. Magn. 29 (2016) 759–769, https://doi.org/10.1007/s10948-015-3339-4.

[30] S. Pongpadung, T. Kamwanna, V. Amornkitbamrung, Effect of fabrication method on the structural and the magnetic properties of copper ferrite, J. Korean Phys. Soc. 68 (2016) 697–704, https://doi.org/10.3938/jkps.68.697.

[31] D. Shishin, T. Hidayat, E. Jak, S.A. Decterov, Critical assessment and thermodynamic modeling of the Cu–Fe–O system, Calphad 41 (2013) 160–179, https://doi.org/10.1016/j.calphad.2013.04.001.

[32] T. Inoue, S. Iida, Specific heats of copper ferrite, J. Phys. Soc. Jpn. (1958) 656A, https://doi.org/10.1143/JPSJ.13.656A.

[33] S. Mallesh, G. Minji, K.H. Kim, Cubic to tetragonal phase transition in CuFe2O4 nanoparticles, J. Magn. 26 (2021) 7–13, https://doi.org/10.4283/JMAG.2021.26.1.007.

[34] S. Mallesh, V. Srinivas, A comprehensive study on thermal stability and magnetic properties of MnZn-ferrite nanoparticles, J. Magn. Magn. Mater. 475 (2019) 290–303, https://doi.org/10.1016/j.jmmm.2018.11.052.

[35] S. Mallesh, P. Mondal, S. Kavita, V. Srinivas, Y.-W. Nam, Effect of Ni substitution and annealing temperature on structural and magnetic properties of MnZn-Ferrites: Cytotoxicity study of ZnO and SiO2 coated core shell structures, article 154648, Appl. Surf. Sci. 605 (2022), https://doi.org/10.1016/j.apsusc.2022.154648.

[36] S. Mallesh, D. Prabu, V. Srinivas, Thermal stability and magnetic properties of MgFe2O4@ZnO nanoparticle, article 056103, AIP Adv. 7 (2017), https://doi.org/10.1063/1.4975355.

[37] N. Obradović, W.G. Fahrenholtz, S. Filipović, D. Kosanović, A. Dapčević, A. Đorđević, I. Balać, V.B. Pavlović, The effect of mechanical activation on synthesis and properties of MgAl2O4 ceramics, Ceram. Int. 45 (2019) 12015–12021, https://doi.org/10.1016/j.ceramint.2019.03.095.

[38] A.V. Khvan, O.B. Fabrichnaya, G. Savinykh, R. Adam, H.J. Seifert, Thermodynamic assessment of the Cu-Fe-O system, J. Ph. Equilib. Diff. 32 (2011) 498–511, https://doi.org/10.1007/s11669-011-9951-5.

[39] M.A. Cobos, P. de la Presa, I. Llorente, A. García-Escorial, A. Hernando, J. A. Jiménez, Effect of preparation methods on magnetic properties of stoichiometric zinc ferrite, article156353, J. Alloy. Compd. 849 (2020), https://doi.org/10.1016/j.jallcom.2020.156353.

[40] P. Villars, K. Cenzual, Pearson's Crystal Data: Crystal Structure Database for Inorganic Compounds, ASM International, Materials Park, 2021.

[41] S. Singhal, S. Barthwal, K. Chandra, XRD, magnetic and Mössbauer spectral studies of nano size aluminum substituted cobalt ferrites ($CoAl_xFe_{2-x}O_4$), J. Magn. Magn. Mater. 306 (2006) 233–240, https://doi.org/10.1016/j.jmmm.2006.03.023.

[42] G. Kumar, R.K. Kotnala, J. Shah, V. Kumar, A. Kumar, P. Dhimana, M. Singh, Cation distribution: a key to ascertain the magnetic interactions in a cobalt substituted Mg–Mn nanoferrite matrix, Phys. Chem. Chem. Phys. 19 (2017) 16669–16680, https://doi.org/10.1039/C7CP01993A.

[43] J. Hornstra, Dislocations, stacking faults and twins in the spinel structure, J. Phys. Chem. Solids 15 (1960) 311–323, https://doi.org/10.1016/0022-3697(60)90254-7.

[44] P. Veyssiere, J. Rabier, J. Grilhe, Stacking fault energy computations in oxides with normal and inverse spinel structures, Phys. Status Solidi A 31 (1975) 605–614, https://doi.org/10.1002/pssa.2210310233.

[45] D. Balzar, N. Audebrand, M.R. Daymond, A. Fitch, A. Hewat, J.I. Langford, A. Le Bail, D. Louër, O. Masson, C.N. McCowan, N.C. Popa, P.W. Stephens, B.H. Toby, Size–strain line-broadening analysis of the ceria round-robin sample, J. Appl. Crystallogr. 37 (2004) 911–924, https://doi.org/10.1107/S0021889804022551.

[46] M.A. Cobos, P. de la Presa, I. Llorente, J.M. Alonso, A. García-Escorial, P. Marín, A. Hernando, J.A. Jiménez, Magnetic phase diagram of nanostructured zinc ferrite as a function of inversion degree δ, J. Phys. Chem. C 123 (2019) 17472–17482, https://doi.org/10.1021/acs.jpcc.9b02180.

[47] A. Younes, N. Kherrouba, A. Bouamer, Magnetic, optical, structural and thermal properties of copper ferrite nanostructured synthesized by mechanical alloying, Micro Nano Lett. 16 (2021) 251–256, https://doi.org/10.1049/mna2.12040.

[48] F. Kenfack, H. Langbein, Influence of the temperature and the oxygen partial pressure on the phase formation in the system Cu – Fe – O, Cryst. Res. Technol. 39 (2004) 1070–1079, https://doi.org/10.1002/crat.200410292.

[49] S.S. Alexandre, E. Anglada, J.M. Soler, F. Yndurain, Magnetism of two-dimensional defects in Pd: stacking faults, twin boundaries, and surfaces, article 054405, Phys. Rev. B (2006), https://doi.org/10.1103/PhysRevB.74.054405.

[50] F. Yndurain, L.M. Falicov, Electronic structure of stacking faults in transition metals: Nickel, Phys. Rev. Lett. 37 (1976) 928–930, https://doi.org/10.1103/PhysRevLett.37.928.

[51] A. Rečnik, I. Nyirő-Kósa, I. Dódonyc, M. Pósfai, Growth defects and epitaxy in Fe3O4 and γ-Fe2O3 nanocrystals, CrystEngComm 15 (2013) 7539–7547, https://doi.org/10.1039/c3ce40873f.

[52] V.A.M. Brabers, J. Klerk, Dilatometric investigation of the phase transition in copper ferrite, Thermochim. Acta 18 (1977) 287–294, https://doi.org/10.1016/0040-6031(77)85062-4.

[53] M.J. Klein, On a Degeneracy Theorem of Kramers, Am. J. Phys. 20 (1952) 65–71, https://doi.org/10.1119/1.1933118.